



Cite this: *Nanoscale Adv.*, 2024, **6**, 6386

MoS₂ quantum dot-decorated CNT networks as a sulfur host for enhanced electrochemical kinetics in advanced lithium–sulfur batteries†

Meng Wei, *^{ab} Hanqing Lu,^a Zhen Wang,^a Baowen Lu,^a Pengtao Wang,^a Xinxin Zhang,^a Bingjie Feng,^a Yingjie Xie,^a Tao Zhang,^a Guanghui Liu^a and Song Xu^{*a}

The slow redox kinetics and shuttle effect of polysulfides severely obstruct the further development of lithium–sulfur (Li–S) batteries. Constructing sulfur host materials with high conductivity and catalytic capability is well acknowledged as an effective strategy for promoting polysulfide conversion. Herein, a well-designed MoS₂ QDs–CNTs/S@Ni(OH)₂ (labeled as MoS₂ QDs–CNTs/S@NH) cathode was synthesized via a hydrothermal process, in which conductive polar MoS₂ quantum dot-decorated carbon nanotube (CNT) networks coated with an ultrathin Ni(OH)₂ layer acted as an efficient electrocatalyst. MoS₂ QD nanoparticles with a high conductivity and catalytic nature can enhance the kinetics of polysulfide conversion, expedite Li₂S nucleation, and decrease the reaction energy barrier. The thin outer Ni(OH)₂ layer physically confines active sulfur and meanwhile provides abundant sites for adsorption and conversion of polysulfides. Benefiting from these merits, a battery using MoS₂ QDs–CNTs/S@NH as the sulfur host cathode exhibits excellent electrochemical performances with rate capabilities of 953.7 mA h g^{−1} at 0.1C and 606.6 mA h g^{−1} at 2.0C. A prominent cycling stability of a 0.052% decay rate per cycle after 800 cycles is achieved even at 2C.

Received 24th January 2024
Accepted 18th October 2024

DOI: 10.1039/d4na00068d
rsc.li/nanoscale-advances

1 Introduction

Rapid global energy growth and a low-carbon economy have driven the vigorous development of higher energy-density devices.^{1,2} Almost every portable device, such as smart grids, portable electronics, and electric vehicles, that use electricity has benefited from the development of rechargeable lithium-ion batteries (LIBs).^{3,4} However, the most advanced commercial lithium-ion battery nearly reaches its theoretical limitation owing to the “Li⁺ intercalation” mechanism, which restricts its developing potential in competitive future application.^{5,6} In order to accomplish the goal of high energy density over 500 W h kg^{−1}, it is an urgent need to explore new battery systems.^{7,8} In this case, lithium–sulfur (Li–S) batteries with a high theoretical energy density of 2600 W h kg^{−1}, environmentally friendly nature and abundant reserves of sulfur have been regarded as the promising candidate for next generation batteries.^{9,10}

However, the application of Li–S batteries is still challenging. There are several technical problems that have not been solved, such as sluggish reaction kinetics, dielectric sulfur and its final product Li₂S, soluble lithium polysulfides (LiPSs), and sulfur volume expansion.^{11,12} The most serious one is the dissolution of polysulfides and their shuttling effect (the so-called shuttle effect) caused by soluble lithium polysulfides (LiPSs), which can shuttle between the cathode and Li anode, resulting in the loss of active materials and low utilization of active sulfur.^{13,14} The dissolution of long-chain LiPSs not only increases the viscosity of the electrolyte, but also increases charge transfer resistance.¹⁵ Moreover, with the soluble LiPSs forming the nucleation barrier of solid Li₂S₂/Li₂S, parts of them are lost from the electrode, leading to incapable transformation from liquid high-order lithium polysulfides (Li₂S_n, 4 ≤ n ≤ 8) to solid lithium polysulfides (Li₂S_n, 1 ≤ n ≤ 2) under high current density.^{16,17} Meanwhile, the converse transition of solid Li₂S to dissolved LiPSs needs to overcome additional activation energy due to the aggregation of Li₂S produced. Solid–liquid–solid phase transitions and their sluggish kinetic conversion problems sharply reduce the capacity, cycling life, and coulombic efficiency of Li–S batteries.^{18,19}

Traditional physical confinement and chemisorption have been proven effective in dealing with the shuttle effect; however, they only alleviate the polysulfide shuttling to some extent and cannot solve the problem fundamentally.^{20,21} The root cause of

^aSchool of Materials Science and Engineering, Zhengzhou University of Aeronautics, Zhengzhou 450046, China. E-mail: weimeng1005@zua.edu.cn; songxu@zua.edu.cn

^bCollaborative Innovation Center of Aviation Economy Development, Henan Province, China

† Electronic supplementary information (ESI) available. See DOI: <https://doi.org/10.1039/d4na00068d>

the shuttle effect is the slow transformation of the liquid phase intermediate lithium polysulfide (Li_2S_n , $4 \leq n \leq 8$) to solid product $\text{Li}_2\text{S}_2/\text{Li}_2\text{S}$, which continuously accumulates in the cathode and diffuses to the lithium anode driven by the concentration gradient and electric field.^{22,23} The electrochemical reaction kinetics can likely slow down inside the battery. Hence, a new perspective of electrocatalytic reaction kinetics that accelerates the sulfur “solid–liquid–solid” conversion process will be required.^{24–27}

Enormous endeavors have been made to overcome this issue. Conductive materials (*e.g.*, carbon-based materials,^{28–31} metal oxides,^{32,33} conductive polymers³⁴) have been widely used as the host materials to construct a conductive network and weaken the dissolution of polysulfide. However, the low-polar carbon materials are limited to weak interactions with LiPSs and can only trap LiPSs by physical confinement and chemical adsorption, which cannot effectively suppress the shuttle effect and promote the conversion kinetics of the battery.^{35,36} In this case, polar metal compounds with strong adsorption capacity for LiPSs have been developed successively to promote ion adsorption and migration efficiently, such as VS_2 ,³⁷ TiS_2 ,³⁸ WS_2 ,³⁹ ReS_2 ,⁴⁰ TiO_2 ,⁴¹ MnO_2 ,⁴² VO_2 ,⁴³ VN ,^{44,45} and so on. Among these, molybdenum disulfide (MoS_2), with the change of lattice plane, high surface area and plentiful active sites, facilitates the strengthening of the overall absorption of Mo ions with negatively charged polysulfides.⁴⁶ Meanwhile, MoS_2 is a typical two-dimensional transition metal sulfide that forms zero-dimensional MoS_2 quantum dots (MoS_2 QDs) when the MoS_2 QDs size is reduced to 10 nm and below. The advantages such as unsaturated bonds, strong binding energy, and abundant polar active sites are expected to greatly enhance the kinetics of polysulfides redox reactions.⁴⁷

Herein, a novel architecture of MoS_2 QDs-CNTs/S@NH was constructed to accommodate sulfur, followed by ultrathin $\text{Ni}(\text{OH})_2$ layer encapsulation. The MoS_2 QDs-CNTs/S@NH cathode was prepared by a hydrothermal process, in which nanosized MoS_2 QDs anchored on CNTs networks were used in both the sulfur host and multifunctional electrocatalysts to catalyze the LiPSs conversion. Benefiting from the synergy between conductive MoS_2 QDs-CNTs framework and ultrathin $\text{Ni}(\text{OH})_2$ layer coating, the shuttle effect was effectively suppressed, and catalytic conversion of polysulfides showed a significant improvement. The MoS_2 QDs-CNTs/S@NH-fabricated batteries with a high sulfur content of 70 wt% show excellent performance both in long cycling stability and rate capability. The MoS_2 QDs-CNTs/S@NH cathode offers enhanced performance with an excellent capacity retention of 59.2% over 800 cycles at 2C. The improved electrochemical performance can be attributed to the design of the cathode, whose CNTs network provides fast electron/ion transfer and polar MoS_2 QDs offering lots of active sites to adsorb polysulfides through chemical interactions. The thin $\text{Ni}(\text{OH})_2$ layer coats as a physically protective shield, not only confining active sulfur but also effectively inhibiting polysulfides shuttle through chemical interactions.

2 Experimental section

2.1 Materials

Molybdenum disulfide (Analytical pure, Shanghai Aladdin Reagent Co., Ltd.); nickel sulfate hexahydrate (AR, 99.9%), ammonium persulfate (AR, 98%) (all analytically pure, Shanghai Aladdin Biochemical Technology Co., Ltd.), ammonia solution (Analytically pure, Xi long Chemical Co., Ltd.), carbon nanotube multi-walled carbon nanotubes (ID: 5–10 nm, OD: 20–30 nm, length: 10–30 nm), sublimed sulfur, *N*-methyl pyrrolidone (NMP) (all analytically pure, Sinopharm Group Chemical Reagents Co., Ltd.); lithium sulfide, thioacetamide 1,3-dioxane (DOL), ethylene glycol dimethyl ether (DME) (Analytically pure, Shanghai Aladdin Reagent Co., Ltd.); LA133 Water system binder (Guangdong Candle New Energy Technology Co., Ltd.).

2.2 Preparation of MoS_2 QDs

Typically, methanol aqueous solution (40 vol%) and ethanol aqueous solution (45 vol%) were mixed in a volume ratio of 1 : 1. 100 mg of molybdenum disulfide powder was dispersed in 40 mL methanol/ethanol solution and ultrasonically treated at room temperature for 2 h. Then, the mixture was dispersed in an ultrasonic cell crusher for 2 h with low-temperature control. After centrifugation at 11 000 rpm for 10 min 3 times, the MoS_2 QDs were obtained and stored at 4 °C.

2.3 Preparation of MoS_2 QDs-CNTs

0.15 g of hydroxylated carbon nanotubes were dispersed in 50 mL distilled water and sonicated for 30 min. Subsequently, the molybdenum disulfide quantum dot (MoS_2 QDs) solution was uniformly mixed into the CNTs dispersion and stirred for 45 min (mass ratio of 50 : 1 for CNTs to MoS_2 QDs). The mixture was poured into a 100 mL hydrothermal reactor and reacted for 12 h at 180 °C. After cooling to room temperature, the resulting material is extracted and filtered, then washed several times with deionized water and ethanol to remove surface impurities. Finally, the experimental material was freeze-dried for 24 h to obtain a pure MoS_2 QDs-CNTs sample.

2.4 Preparation of MoS_2 QDs-CNTs/S

MoS_2 QDs-CNTs/S composite material was prepared using a simple melt diffusion method. MoS_2 QDs-CNTs and sublimed sulfur were mixed in a mass ratio of 3 : 7, and the mixture was ground for 40 min. Subsequently, the mixture was transferred to a stainless steel reactor and heated at 155 °C in an argon atmosphere for 12 h. After cooling to room temperature, the MoS_2 QDs-CNTs/S composite material was obtained.

2.5 Preparation of MoS_2 QDs-CNTs/S@NH

The $\text{Ni}(\text{OH})_2$ layer was coated on the surface of the MoS_2 QDs-CNTs/S precursor using a surface chemical precipitation method. The mixed solution was formed by dispersing 4 mL nickel sulfate hexahydrate and 2.5 mL ammonium persulfate in 100 mL deionized water. Subsequently, 0.45 g MoS_2 QDs-CNTs/S composite was dissolved in the mixed solution to form a stable



solution. Then, 10 mL of concentrated ammonia solution was added, followed by stirring at room temperature for 30 min and standing for 20 min. The product was centrifuged at 5000 rpm for 10 min and washed several times. Finally, the MoS₂ QDs-CNTs/S@NH material was obtained after drying in a vacuum oven at 60 °C for 12 h.

2.6 Preparation of the MoS₂ QDs-CNTs/S@NH cathode

The MoS₂ QDs-CNTs/S@NH composite with conductive carbon black was mixed uniformly in a mass ratio of 8 : 1. Subsequently, the powder was added to the LA133 solution in a weight ratio of 9 : 1 and stirred for 12 h to prepare a homogeneous slurry. The prepared slurry was coated onto an aluminum foil with a thickness of 300 μm and subsequently dried in a vacuum drying oven for 12 h. After drying, the MoS₂ QDs-CNTs/S@NH cathode was cut into disks with a diameter of 12 mm for assembly into CR2032 coin cells.

2.7 Material characterization

The crystallinity and structure of the samples were characterized using X-ray diffraction (XRD) with a Bruker D2 PHASER instrument. Scanning electron microscopy (SEM) utilizing the ZEISS Gemini 300 and transmission electron microscopy (TEM) employing the JEOL JEM-2100Plus were employed to characterize the morphology and structure of the samples. X-ray photoelectron spectroscopy (XPS) measurements were conducted to analyze the chemical states of elements and material composition. The sulfur content in the MoS₂ QDs-CNTs/S@NH composite was characterized using a thermogravimetric analyzer (TG, TG 209F3). The concentration of Li₂S₆ in the solution was characterized using a UV-visible spectrophotometer (UV-vis, UV-5500PC), facilitating the analysis of lithium polysulfide adsorption properties in the samples.

2.8 Electrochemical measurements

The MoS₂ QDs-CNTs/S@NH composite, conductive superphosphate and binder LA133 were mixed in a ratio of 7 : 2 : 1 to form a uniform slurry. The slurry was cast onto an aluminum foil, vacuum-dried at 60 °C for 12 h and subsequently punched into discs with a diameter of 12 mm. The coin cells were assembled with MoS₂ QDs-CNTs/S@NH as the cathode, Celgard 2500 as the separator, lithium foil as the anode and 1 M LiTFSI solution in a mixed solvent of 1,3-dioxolane (DOL) and 1,2-dimethoxyethane (DME) in a volume ratio of 1 : 1 in a glove box filled with Ar (H₂O, O₂ < 0.1 ppm). The sulfur content of the whole cathode is approximately 70 wt%. The sulfur mass loading on the cathode ranges between 2 and 2.7 mg cm⁻². Furthermore, the ratio of the cathode electrolyte to sulfur is 13 μL mg⁻¹. The electrochemical performance of the system was characterized using the LAND testing system and CHI-604E electrochemical workstation. Cyclic voltammetry (CV) was tested at a scan rate of 0.1 mV s⁻¹, and electrochemical impedance spectroscopy (EIS) was performed by a frequency range of 100 kHz to 0.01 Hz.

3 Results and discussion

The synthetic process of the MoS₂ QDs-CNTs/S@NH material is illustrated in Fig. 1. The MoS₂ QDs-CNTs/S@NH shows an effective design with CNTs constructed as a conductor network and MoS₂ QDs homogeneously and tightly anchored on the CNTs networks. The active sulfur is loaded on the surface of the CNTs network, and a thin Ni(OH)₂ layer is coated outside as a protective shield.

Fig. 2(a)–(d) illustrates the morphological evolution process of the CNTs powder, MoS₂ QDs-CNTs, MoS₂ QDs-CNTs/S and MoS₂ QDs-CNTs/S@NH, respectively. As shown in Fig. 2(a), the surface of naked carbon nanotubes (CNTs) is extremely smooth,

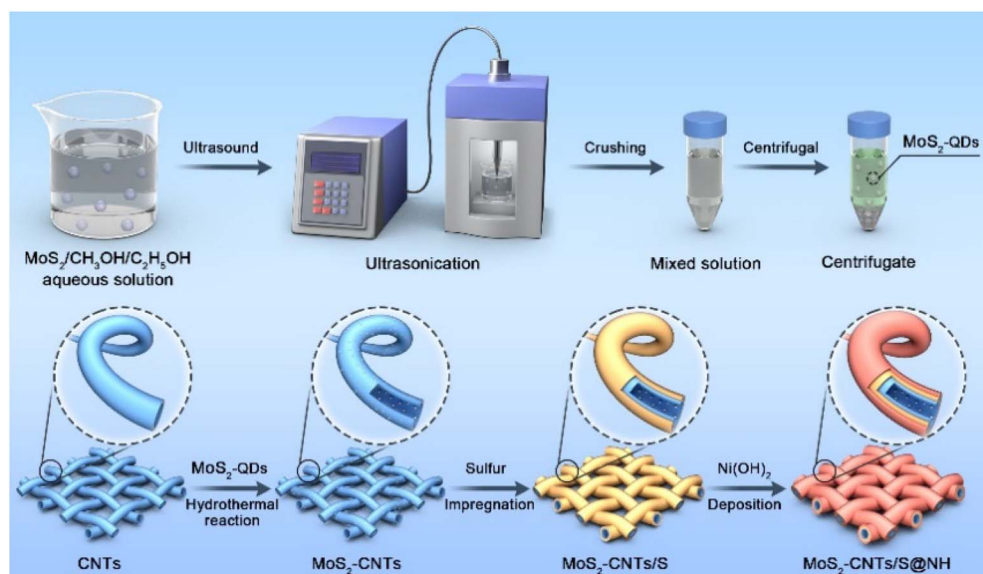


Fig. 1 Schematic of the synthesis process of MoS₂ QDs-CNTs/S@NH composites.



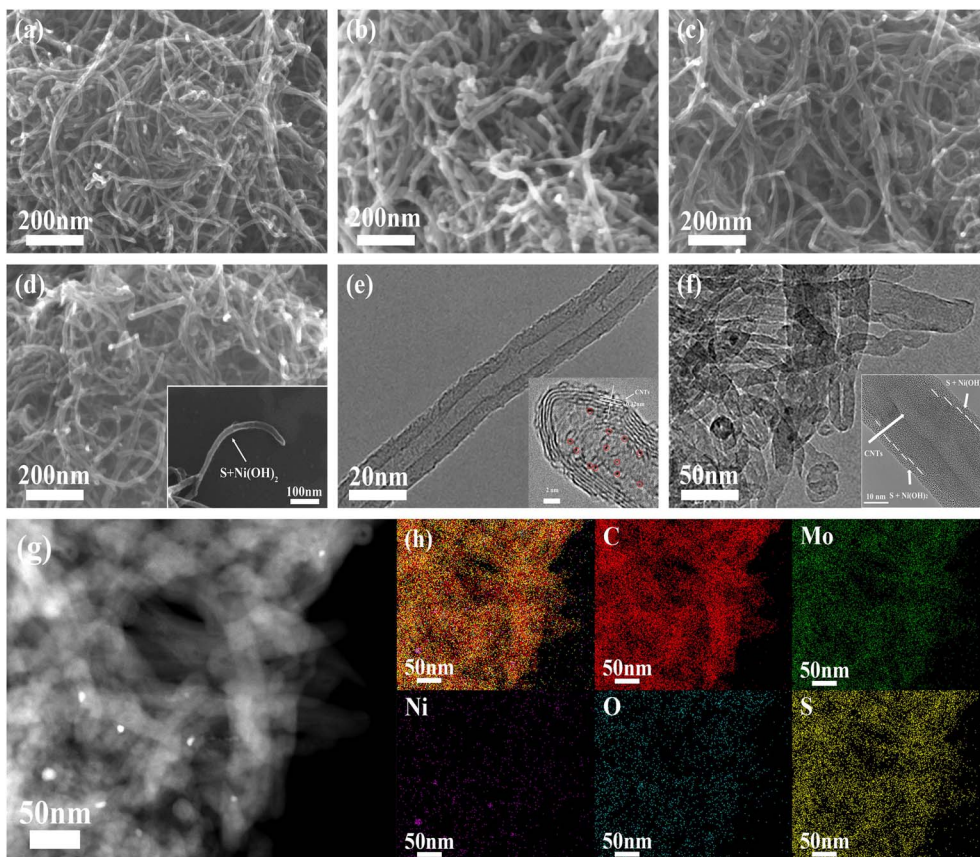


Fig. 2 SEM images of (a) CNTs, (b) MoS₂ QDs-CNTs, (c) MoS₂ QDs-CNTs/S, and (d) MoS₂ QDs-CNTs/S@NH. (e) HRTEM image of MoS₂ QDs-CNTs. (f and g) High-magnification TEM image of MoS₂ QDs-CNTs/S@NH and the EDS mapping.

with an outer diameter of approximately 30–40 nm+. Through the hydrothermal reaction process, MoS₂ quantum dots (QDs) were successfully decorated onto the surface of carbon nanotubes, forming the MoS₂ QDs-CNTs composite shown in Fig. 2(b). Compared to the bare carbon nanotubes, the MoS₂ QDs-CNTs sample exhibits a relatively rough surface while preserving its initial one-dimensional structure. The MoS₂ QDs-CNTs/S sample was prepared *via* the sulfur impregnation method, as shown in Fig. 2(c). The surface of MoS₂ QDs-CNTs/S becomes slightly smoother than MoS₂ QDs-CNTs, which can be attributed to the fact that MoS₂ quantum dots (QDs) on the surface have been covered after sulfur loading. To further suppress the shuttle effect of polysulfides, the MoS₂ QDs-CNTs/S composite was subsequently coated with a thin Ni(OH)₂ layer. From Fig. 2(d) and the inset, a polar layer of Ni(OH)₂ is clearly coated onto the surface of the MoS₂ QDs-CNTs/S sample, achieving the successful construction of a core–shell structured MoS₂ QDs-CNTs/S@NH cathode. Fig. 2(e) shows the high-resolution transmission electron microscope (HRTEM) image of MoS₂ QDs-CNTs in which small MoS₂ QDs (<5 nm) are evenly decorated on the surface of carbon nanotubes and some are encapsulated in narrow channels. The HRTEM is further proof of the coexistence of MoS₂ QDs and CNTs. HRTEM images (Fig. 2(e)) show highly parallel and ordered lattice fringes, demonstrating the MoS₂ QDs are well crystallized. The *d*-

spacing of MoS₂ QDs is 0.25 nm due to the (103) faces of MoS₂ crystals. From the TEM image in Fig. 2(f) and the insertion, it is clear that the MoS₂ QDs-CNTs nucleus is surrounded by a thin Ni(OH)₂ shell. The high-magnification TEM image (Fig. 2(f)) confirms the nanosized MoS₂ QDs decorated on the network structure of carbon nanotubes and coated by a thin Ni(OH)₂ layer, which coincides with the SEM image in Fig. 2(d).

The as-prepared MoS₂ QDs-CNTs/S and its energy dispersive X-ray (EDX) analysis are also investigated (Fig. S1†). After coating with Ni(OH)₂, the MoS₂ QDs-CNTs/S@NH and corresponding EDS mappings are shown in Fig. 2(g). Fig. 2(g) depicts the C, Ni, Mo, S and O elements detected in the MoS₂ QDs-CNTs/S@NH composite material, which demonstrates a homogeneous distribution of elements (C, O, Mo, S) in composites and the presence of the Ni(OH)₂ layer. The additional Ni(OH)₂ layer not only prevents the migration of sulfur but also facilitates the polar chemical adsorption to immobilize the dissolved polysulfides.

X-ray diffraction (XRD) was performed to evaluate the purity and crystalline phases of the sample. To ensure the successful synthesis of MoS₂ QDs-CNTs/S@NH, pure MoS₂ QDs and Ni(OH)₂ were both prepared and tested. As shown in Fig. 3(a), the diffraction peaks at 19.25°, 33.06° and 38.54° correspond to the (001), (100) and (101) planes of Ni(OH)₂, confirming the successful preparation of nickel hydroxide.⁴⁸ However, clear



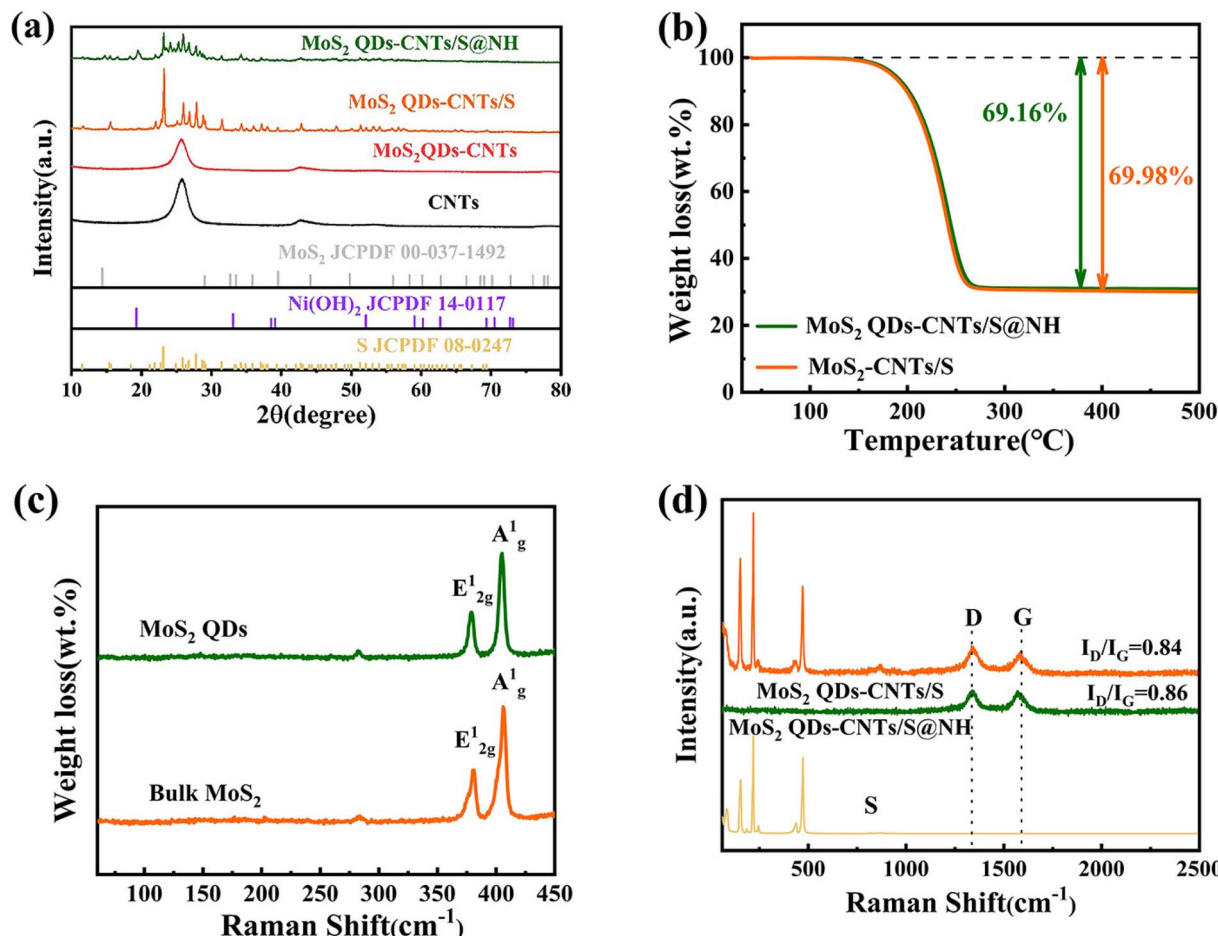


Fig. 3 (a) XRD patterns of S, CNTs, MoS₂ QDs-CNTs, Ni(OH)₂, MoS₂ QDs-CNTs/S and MoS₂ QDs-CNTs/S@NH composite materials; (b) TG curves of MoS₂ QDs-CNTs/S and MoS₂ QDs-CNTs/S@NH; (c) Raman spectra of MoS₂ QDs and bulk MoS₂. (d) Raman spectra of MoS₂ QDs-CNTs/S and MoS₂ QDs-CNTs/S@NH.

peaks related to molybdenum disulfide (MoS₂) were not detected in the XRD spectrum of MoS₂ QDs-CNTs. This can be attributed to the low mass ratio of MoS₂ QDs as well as the incorporation of some MoS₂ QDs into the lattice of carbon nanotubes without altering the crystal structure. The strong diffraction peaks of sublimed sulfur are detected in MoS₂ QDs-CNTs/S and MoS₂ QDs-CNTs/S@NH composites, indicating the presence of a well-defined S₈ crystal structure (S JCPDS 08-0247). While the Ni(OH)₂ was coated, it was noted that no distinct diffraction peaks of Ni(OH)₂ were observed in the MoS₂ QDs-CNTs/S@NH sample, which could be attributed to either a low content of Ni(OH)₂ or the overlapping of weak Ni(OH)₂ peaks with the strong diffraction peaks of sulfur. The intensity of the sulfur peaks was relatively weaker in MoS₂ QDs-CNTs/S@NH due to the Ni(OH)₂ layer, which agrees with the Raman analysis. The sulfur content of the MoS₂ QDs-CNTs/S and MoS₂ QDs-CNTs/S@NH samples was confirmed by thermogravimetric analysis (TGA). As shown in Fig. 3(b), a weight loss of 69.98% for the MoS₂-CNTs/S sample can be observed when the temperature increases to 300 °C, which can be attributed to the evaporation of sulfur. For MoS₂ QDs-CNTs/S@NH, approximately 69.16% sulfur loss was observed, slightly lower than that

of MoS₂ QDs-CNTs/S. This slight difference can be attributed to the decomposition of Ni(OH)₂. Such low content of Ni(OH)₂ is in accord with the fact that the diffraction peak of Ni(OH)₂ was undetectable in the XRD analysis.

Raman spectroscopy was conducted to study the microstructure of bulk MoS₂, MoS₂ QDs, MoS₂ QDs-CNTs/S and MoS₂ QDs-CNTs/S@NH. In Fig. 3(c), the characteristic peaks A_g¹ and E_{2g}¹ of MoS₂ QDs were perfectly consistent with the peaks of bulk MoS₂, which are located at 406.7 cm⁻¹ and 381 cm⁻¹.^{49,50} The Raman spectrum of MoS₂ QDs-CNTs/S and MoS₂ QDs-CNTs/S@NH with two main modes, the D and the G band were located at 1337 cm⁻¹ and 1573 cm⁻¹, which reveals the disordered vibration of carbon atoms with defects and two-dimensional vibration in the hexagonal lattice of sp²-bonded carbon atoms (Fig. 3(d)). In general, the relative intensity ratio I_D/I_G is an indication of the carbon nanotube quality. The I_D/I_G value of MoS₂ QDs-CNTs/S@NH (I_D/I_G 0.86) is smaller than that of MoS₂ QDs-CNTs/S (I_D/I_G 0.84), indicating that combine with Ni(OH)₂ does not affect the defects material after the sonication or hydrothermal process. The characteristic Raman peak of sulfur was observed on MoS₂ QDs-CNTs/S, and three sharp peaks of the S/CNT/G film below 600 cm⁻¹ could be assigned to



the S-S bond in the composites. It is noteworthy that the Raman spectra of MoS_2 QDs-CNTs/S@NH showed no sulfur peak, indicating that S_8 molecules were well fixed in the $\text{Ni}(\text{OH})_2$ thin layer without significant molecular vibrations. This result further proves that the structure of $\text{Ni}(\text{OH})_2$ on the surface of sulfur can well limit the diffusion of sulfur, thereby improving the utilization rate and stability of sulfur.

X-ray photoelectron spectroscopy (XPS) was employed to further investigate the chemical composition and surface

electric states of the elements in the MoS_2 QDs-CNTs/S@NH composite. In the overall survey spectrum of Fig. 4(a), the presence of C, O, S, Mo and Ni identifies the existence of these elements in the composite. Fig. 4(b)–(f) display the high-resolution XPS spectra for C 1s, O 1s, Mo 3d, Ni 2p and S 2p of MoS_2 QDs-CNTs/S@NH, respectively. As shown in Fig. 4(b), the C 1s spectrum can be deconvoluted into four peaks at 284.7, 285.59, 286.28 and 287.88 eV, which corresponded to the C-C/C=C, C-O/C-S, C-O and O-C=O bonds. The existence of S-C

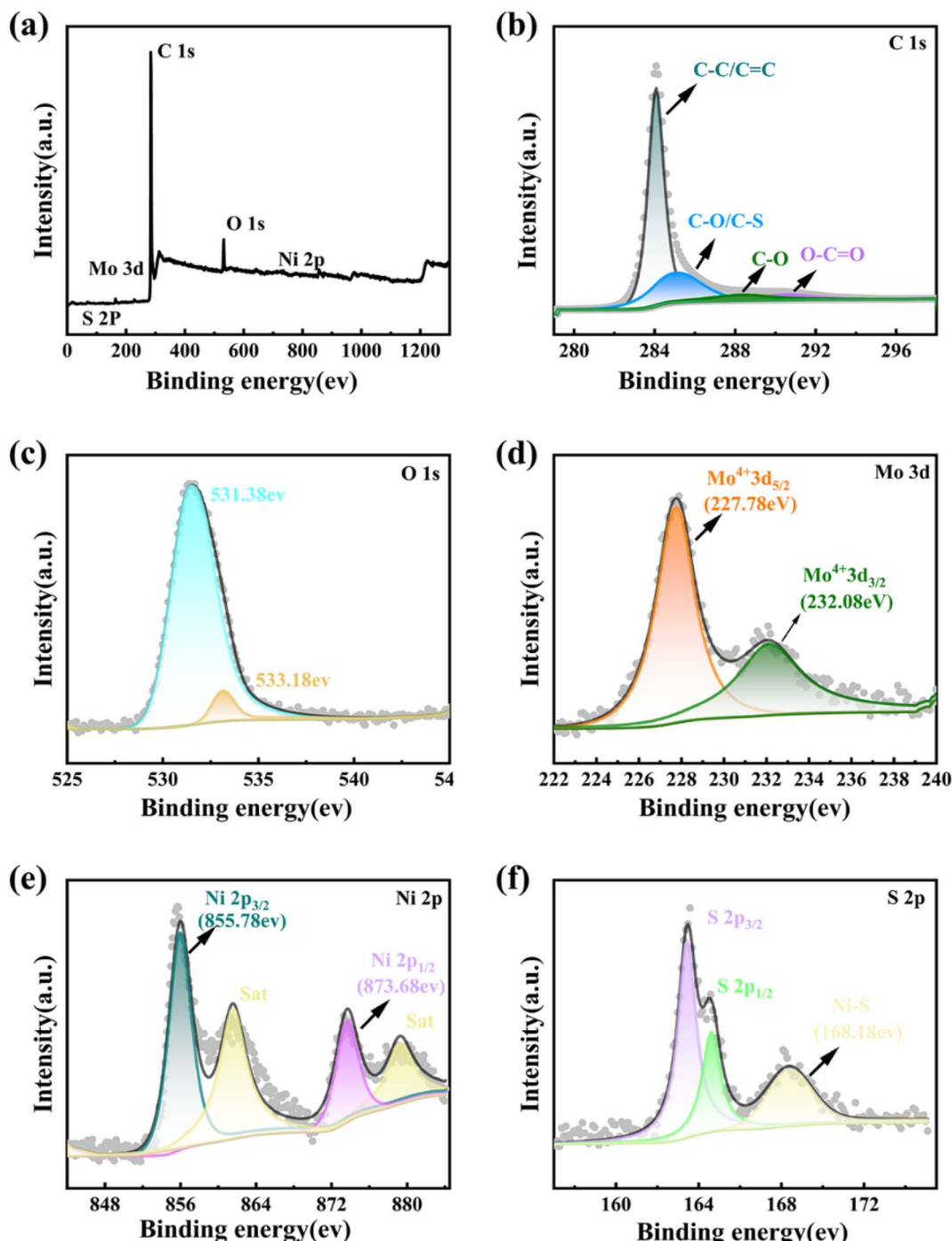


Fig. 4 XPS spectra of the MoS_2 QDs-CNTs/S@NH sample: (a) overall XPS spectrum, (b) C 1s, (c) O 1s, (d) Mo 3d, (e) Ni 2p, and (f) S 2p XPS spectra.



brings out the strong interactions between sulfur and the carbon matrix.⁵¹ In Fig. 4(c), the peak located at the binding energy of 531.38 eV in the O 1s spectrum can be ascribed to the formation of O-H bonds in Ni(OH)₂. Fig. 4(d) displays the binding energies of Mo 3d_{5/2} and Mo 3d_{3/2} in the material at 227.78 eV and 232.08 eV, respectively. In Fig. 4(e), two prominent peaks of the Ni 2p XPS spectrum labeled as Ni 2p_{3/2} and Ni 2p_{1/2} are located at binding energies of 855.78 eV and 873.68 eV, and the satellite peaks are located at 861.48 eV and 879.38 eV. A change in the chemical valence of Ni indicates that polar Ni(OH)₂ can serve as a medium or catalyst to transform polysulfides, which is beneficial for accelerating the reaction kinetics and enhancing the electrochemical performance.

Fig. 4(f) displays the peaks of S 2p (corresponding to S 2p_{3/2} and S 2p_{1/2}) located at 163.48 eV and 164.58 eV. The S 2p energy spectrum exhibits a high-energy peak at 168.48 eV, which can give credit to the formation of Ni-S chemical bonds, proving the highly efficient suppression of active sulfur by MoS₂ QDs-CNTs/S@NH.

In order to investigate the electrochemical improvements of the Li-S cells using CNTs/S, MoS₂ QDs-CNTs/S and MoS₂ QDs-CNTs/S@NH cathode, cyclic voltammetry (CV) tests were performed at a scan rate of 0.1 mV s⁻¹. Fig. 5(a) illustrates the CV curves of cells using CNTs/S, MoS₂ QDs-CNTs/S and MoS₂ QDs-CNTs/S@NH as positive electrode materials and lithium foil as the negative electrode. For the three samples, one dominant

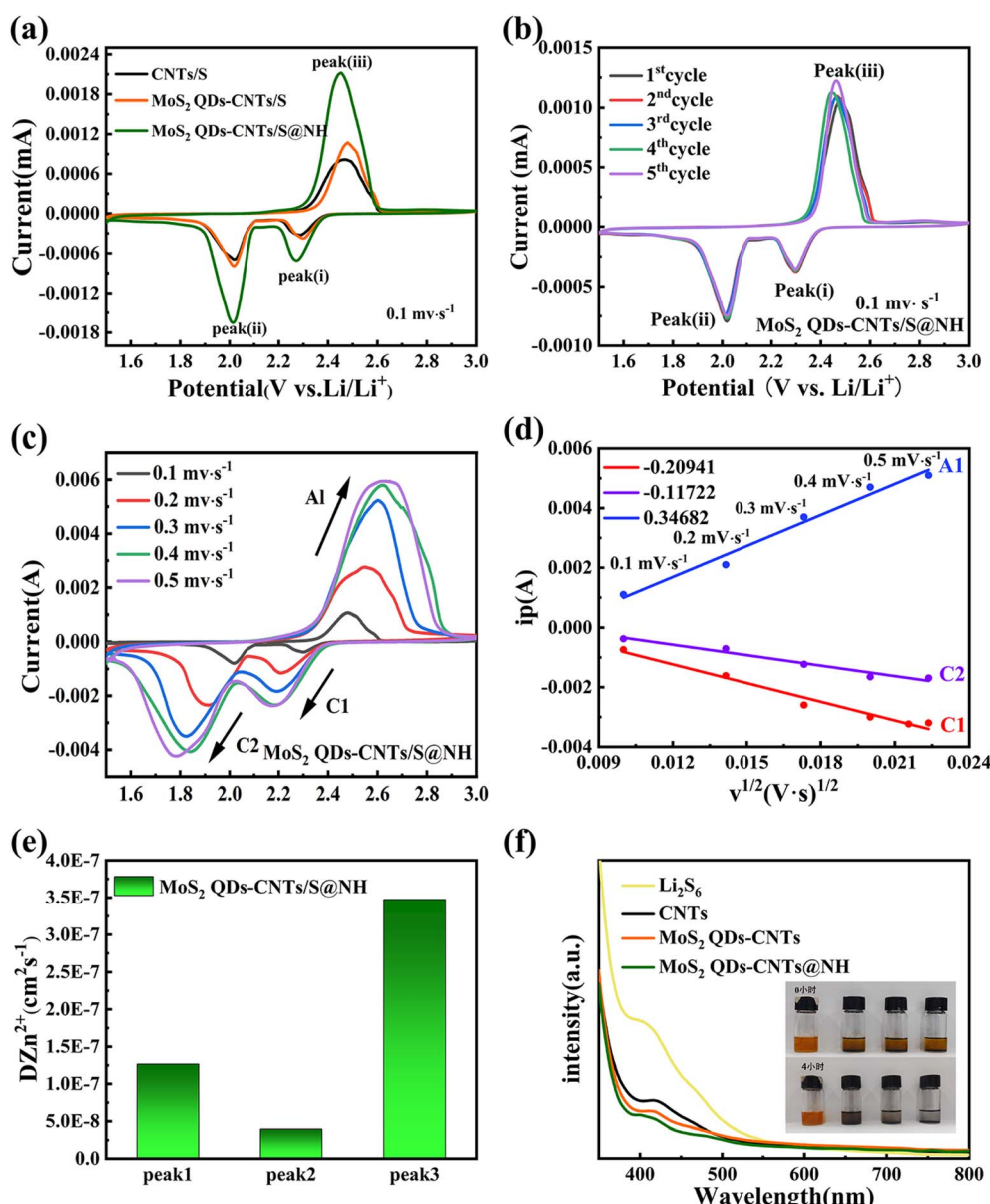


Fig. 5 (a) CV curves of CNTs/S, MoS₂ QDs-CNTs/S, and MoS₂ QDs-CNTs/S@NH cathodes in the potential range of 1.5–3.0 V at 0.1 mV s⁻¹; (b) CV curves at 0.1 mV s⁻¹ for MoS₂ QDs-CNTs/S@NH; (c) CV profiles at different scan rates of MoS₂ QDs-CNTs/S@NH. (d) Plots of CV peak current vs. the square root of the scan rates for MoS₂ QDs-CNTs/S@NH. (e) Impedance value of MoS₂ QDs-CNTs/S@NH. (f) UV-vis spectra and variation in the color of Li₂S₆ solution adsorbed by CNTs/S, MoS₂ QDs-CNTs/S, and MoS₂ QDs-CNTs/S@NH for 4 h.



anodic peak at around 2.45 V corresponds to the oxidation of Li_2S to S_8 , and two reduction peaks were observed at around 2.29 V and 1.9 V during the discharge process, which correspond to the conversion of elemental sulfur (S_8) into long-chain Li_2S_x ($4 < x < 8$), followed by the further reduction of long-chain lithium polysulfides into short-chain lithium polysulfides, and ultimately to insoluble Li_2S_2 and Li_2S .⁵² Comparatively, the reduction peak of MoS_2 QDs-CNTs/S@NH shows a higher potential and the oxidation peak shows a lower potential, exhibiting the smallest potential difference between the reduction and oxidation peaks, which suggests the MoS_2 QDs-CNTs/S@NH has a greater effect on promoting the kinetic reduction of long-chain LiPSs to $\text{Li}_2\text{S}_2/\text{Li}_2\text{S}$ and reducing the polarization of the Li-S battery. Meanwhile, the sharpness and intensity of the peaks are significantly higher, indicating faster LiPSs reaction kinetics and smaller electrochemical polarization ($\Delta V = 0.44$ for MoS_2 QDs-CNTs/S@NH; MoS_2 QDs-CNTs/S $\Delta V = 0.448$; CNTs/S $\Delta V = 0.526$). These results are consistent with the previous results of Li_2S_6 adsorption experiments. Fig. 5(b) illustrates the cyclic voltammetry (CV) curves of MoS_2 QDs-CNTs/S@NH for the first five cycles in the potential range of 1.5–3 V and a scanning rate of 0.1 mV s^{-1} . It can be observed that the first five CV curves overlap well, and the oxidation/reduction peaks exhibit minimal changes, indicating the electrochemical reaction stability during the oxidation–reduction process.

To further investigate the importance of the acceleration of MoS_2 QDs-CNTs/S@NH on Li^+ diffusion, CV tests at different scan rates from 0.1 to 0.5 mV s^{-1} were performed. Fig. 5(c) and (d) presents the CV curves of MoS_2 QDs-CNTs/S@NH at different scanning rates and the corresponding $I-\nu^{1/2}$ fitting lines at each redox current peak. In Fig. 5(c), both the positive and negative electrode currents exhibit a more pronounced increasing trend for MoS_2 QDs-CNTs/S@NH while the scan rate increases, proving the excellent catalytic activity of the MoS_2 QDs-CNTs/S@NH structure due to the polar and catalytic MoS_2 QDs decorated on CNTs and a thin Ni(OH)_2 layer. As shown in Fig. 5(e), the peak current density of MoS_2 QDs-CNTs/S@NH shows a good linear relationship with the square root of the scanning rate, illustrating that the reaction is a Li^+ diffusion-controlled process. According to the Randles–Sevcik equation, the diffusion coefficient of lithium-ion (D_{Li^+}) could be calculated.⁵³ The slopes of $I-\nu^{1/2}$ of MoS_2 QDs-CNTs/S@NH are 0.34682, −0.20941, −0.11722 for peaks A1, C1, C2, suggesting that the MoS_2 QDs-CNTs/S@NH cathode has a much faster Li^+ transport.

The CV results verify that the LiPSs have a high chance of being captured using MoS_2 QDs-CNTs/S@NH as the sulfur host and high-efficiency catalyst. The Mo_2S QD decorated CNTs network structure with a large surface area provides abundant surface active sites to achieve strong interaction with LiPSs. Meanwhile, Mo_2S QDs take advantage of their full catalytic activity, which promotes the electron transfer of CNTs networks and then speeds up the conversion from LiPSs to insoluble Li_2S . Moreover, a thin Ni(OH)_2 layer coats as a physical barrier, not only restricting sulfur loss but also capturing LiPSs through strong chemical interactions. In addition, the Tafel plots of

Mo_2S QDs-CNTs/S@NH are also tested to demonstrate the enhanced conversion kinetics and electrocatalytic activity (Fig. S2†). The MoS_2 QDs-CNTs/S@NH displays a much higher i_0 than that of CNTs. The highest exchange current density is $-3.647 \text{ mA cm}^{-2}$ for the MoS_2 QDs-CNTs/S@NH electrode. Hence, it turns out that the QDs-CNTs/S@NH can effectively accelerate the reversible electrochemical conversion toward LiPSs.

To further showcase this strong interaction between MoS_2 QDs-CNTs/S@NHs and polysulfides, a visualized adsorption experiment in Li_2S_6 solution (0.01 M) was carried out. Fig. 5(f) displays the photograph of the electrolytes from the three types of samples. The electrolyte using CNTs and MoS_2 QDs-CNTs cathode exhibited a pale-yellow color. In contrast, the electrolytes used with the MoS_2 QDs-CNTs/S@NH cathode remain colorless within 2 h, which indicates that the Li_2S_6 in the electrolyte is almost absorbed by MoS_2 QDs-CNTs/S@NH. The comparative experiments show that MoS_2 QDs-CNTs/S@NH exhibits stronger adsorption capacity and good consistency than CNTs and MoS_2 -CNTs. This is because the MoS_2 QDs-CNTs/S@NH can suppress LiPSs dissolution during charge/discharge cycling. As shown in Fig. 5(f), the pure Li_2S_6 solution has a significant adsorption peak at 400 nm, which can be attributed to the S_6^{2-} species. The adsorption strength of UV-vis in the solution with MoS_2 QDs-CNTs/S@NH was significantly reduced, which confirmed that the chemisorption capacity was greatly enhanced by MoS_2 QDs and Ni(OH)_2 coating.⁴⁹

In order to further investigate the solid–liquid conversion and Li_2S deposition kinetics of polysulfides at the electrolyte/electrode interface, the constant potential discharge curves of CNTs and MoS_2 QDs CNTs surfaces were measured using Li_2S_6 as the active substance. As shown in the current time curve in Fig. 6, the dark areas near the X-axis and Y-axis represent the liquid–liquid reduction reactions of Li_2S_6 and Li_2S_8 , respectively, while the light areas represent the liquid–solid conversion reactions of Li_2S deposition. In Fig. 6(b), it is worth noting that the MoS_2 QDs-CNTs have a higher Li_2S deposition ($364.7 \text{ mA h g}^{-1}$) than that of CNTs ($329.7 \text{ mA h g}^{-1}$) (Fig. 6(a)). The results indicated that MoS_2 QDs were beneficial in achieving efficient Li_2S precipitation. The oxidative deposition of Li_2S was further investigated by using a potentiostat, and the dissolved capacity of MoS_2 QDs-CNTs was much higher than that of CNTs during charging at 2.05 V, revealing the effective oxidation of Li_2S on the surface of MoS_2 QDs-CNTs. The catalytic effect of MoS_2 QDs was demonstrated by the results of the potentiostatic discharge curves of CNTs and MoS_2 QDs-CNTs.

The cyclic performance of CNTs/S, MoS_2 QDs-CNTs/S and MoS_2 QDs-CNTs/S@NH at 0.5C is shown in Fig. 7(a). For MoS_2 QDs-CNTs/S@NH, the initial discharge capacity of $1141.4 \text{ mA h g}^{-1}$ and reversible capacity of $884.6 \text{ mA h g}^{-1}$ are obtained after 200 cycles with 77.5% retention. In comparison, the initial discharge capacities of MoS_2 QDs-CNTs/S and CNTs/S are 719.5 and $555.6 \text{ mA h g}^{-1}$. After 200 cycles, their values decrease to 424.1 and $309.8 \text{ mA h g}^{-1}$ (retention rates of 58.9% and 55.7%). The poor cycling stability of CNTs/S is attributed to the lack of an effective barrier for polysulfides and relatively slow sulfur redox reactions. Here, the improved cycling stability



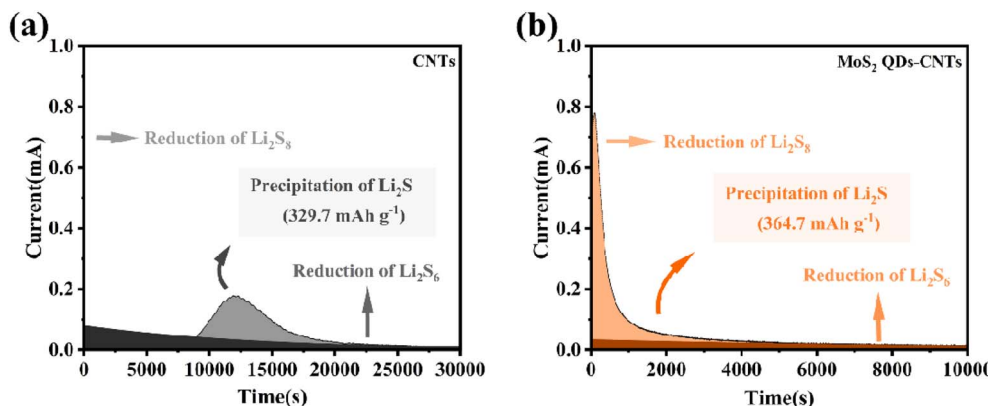


Fig. 6 Potentiostatic discharge curves of CNTs and MoS_2 QDs-CNTs.

of MoS_2 QDs-CNTs/S can be attributed to the designed structure. The CNTs network not only offers rapid electron/ion pathways but also buffers volume changes. The significant number of unsaturated bonds from MoS_2 QDs efficiently anchor polysulfides, while the external Ni(OH)_2 shell not only physically confines the active material but also acts as a barrier layer to suppress the diffusion of polysulfides. In addition, the coulombic efficiency of MoS_2 QDs-CNTs/S@NH during cycling is approximately 99%, which is higher than that of MoS_2 QDs-CNTs/S and CNTs/S.

Fig. 7(b) presents the initial galvanostatic discharge/charge curves of CNTs/S, MoS_2 QDs-CNTs/S and MoS_2 QDs-CNTs/S@NH at 0.2C. Clearly, MoS_2 QDs-CNTs/S@NH exhibits the longest discharge/charge plateau among the three materials, while MoS_2 QDs-CNTs/S displays a moderate but longer discharge/charge plateau compared to CNTs/S. These curves exhibit similar shapes at different current densities, clearly showing two distinct discharge voltage plateaus and one charge voltage plateau. In the discharge curves, the two plateaus at approximately 2.31 V and 2.04 V correspond to the two-stage reactions of sulfur to long-chain polysulfides and then to short-chain sulfides. In the charge-discharge plateaus, the two sloping charge plateaus correspond to the oxidation of $\text{Li}_2\text{S}/\text{Li}_2\text{S}_2$ to $\text{L}_2\text{S}_8/\text{S}$, consistent with the analysis from the CV curves. Additionally, MoS_2 QDs-CNTs/S@NH demonstrates a higher reduction peak potential and a lower oxidation peak potential ($\Delta E = 247.8$ mV). As a result, the electrochemical kinetics in MoS_2 QDs-CNTs/S@NH are greatly enhanced, and the polarization is significantly reduced. Due to the minimal polarization, during the extended discharge plateau, sulfur can be completely converted to insoluble $\text{Li}_2\text{S}_2/\text{Li}_2\text{S}$, thus improving the utilization of active materials and achieving high specific capacity.

Fig. 7(c) displays the rate performance of CNTs/S, MoS_2 QDs-CNTs/S and MoS_2 QDs-CNTs/S@NH cathode at different currents. For MoS_2 QDs-CNTs/S@NH in Fig. 7(d), the reversible discharge/charge capacities provided by the MoS_2 QDs-CNTs/S@NH cathode are 1061.1/1539.2, 893.7/1201.5, 768.1/1053.9, 697.9/103 and 614.4/941.1 at 0.1, 0.2, 0.5, 1.0 and 2.0C, respectively. When the current density returns to 0.1C, the discharge capacity of the MoS_2 QDs-CNTs/S@NH recovers to

797.4 mA h g^{-1} , demonstrating good reversible capacity. In contrast, both MoS_2 QDs-CNTs/S and CNTs/S exhibit significantly lower capacities at the same current rate. Clearly, MoS_2 QDs-CNTs/S@NH displays the best rate performance. The superior rate performance of MoS_2 QDs-CNTs/S@NH can be primarily attributed to the dual suppression effect, and the dissolution and diffusion of polysulfides are dually suppressed by the internal MoS_2 QDs and the external Ni(OH)_2 shell.

For more information about the kinetics of charge transfer and ion diffusion of CNTs/S, MoS_2 QDs-CNTs/S, and MoS_2 QDs-CNTs/S@NH cathodes, electrochemical impedance spectroscopy (EIS) was performed. The corresponding results are displayed in Fig. 7(f). The intersection of the plots on the real axis represents the equivalent series resistance (R_s), which includes the electrolyte resistance, the contact resistance and the resistance of the electrode. All three EIS spectra consist of a single semicircle in the high-frequency region and an inclined line in the low-frequency region. The high-frequency semicircle represents the charge transfer resistance (R_{ct}), and the diagonal line in the low-frequency region is attributed to the Warburg impedance caused by Li^+ diffusion in the electrode. Part of the irreversible Li_2S caused the capacity loss, so the R_s can represent the effectiveness of the redox reaction in the cathode. Clearly, CNTs/S exhibits a relatively high R_s value of 24 Ω , while MoS_2 QDs-CNTs/S and MoS_2 QDs-CNTs/S@NH demonstrate significantly lower R_s values. Thus, the charge transfer resistance (R_{ct}) of MoS_2 QDs-CNTs/S@NH (16 Ω) is lower than that of MoS_2 QDs-CNTs/S (21 Ω) and CNTs/S (24 Ω). The minimum R_{ct} implies the highest electronic conductivity and ionic migration rate between the SEI and electrolyte. These results indicate that constructing a unique core-shell structure of MoS_2 QDs-CNTs/S@NH can accelerate charge transfer kinetics and inhibit the diffusion of polysulfides.

The long cycling performance of the MoS_2 QDs-CNTs/S@NH cathode at high current densities was also investigated. As shown in Fig. 7(g), the MoS_2 QDs-CNTs/S@NH cathode exhibits a capacity of 511.2 mA h g^{-1} and a reversible capacity of 302.2 mA h g^{-1} after 800 cycles at 2C. On average, it retains a capacity retention rate of 59.2%, and a negligible capacity decay of 0.051% per cycle. In addition, the average coulombic



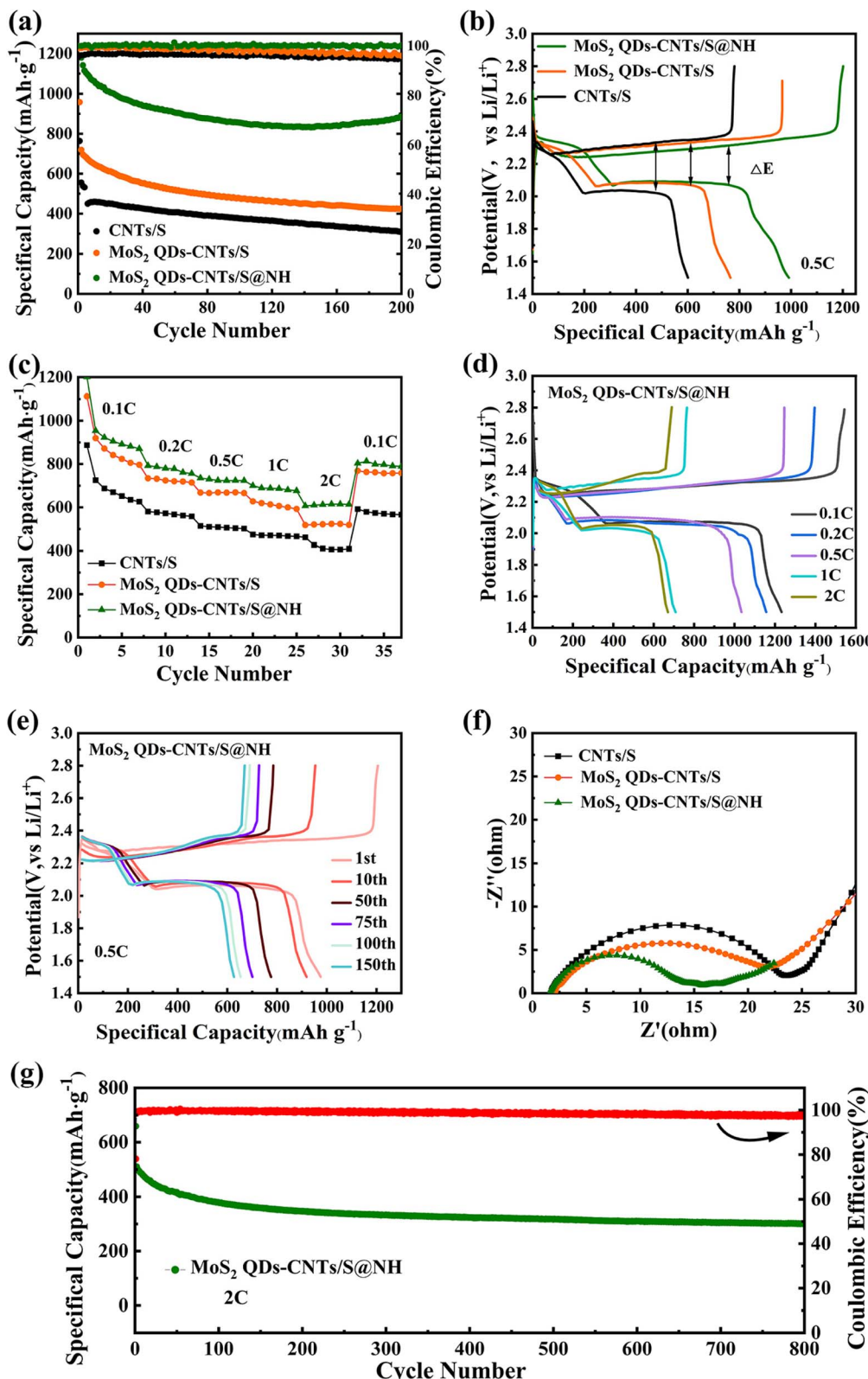


Fig. 7 The electrochemical performance of CNTs/S, Mo₂ QDs-CNTs/S and Mo₂ QDs-CNTs/S@NH. (a) Cycling performance and coulombic efficiency at 0.5C during 200 cycles, (b) initial discharging/charging curves, and (c) rate capabilities of CNTs/S, Mo₂ QDs-CNTs/S and Mo₂ QDs-CNTs/S@NH. (d) Galvanostatic charge-discharge profiles at different rates. (e) Galvanostatic charge-discharge profiles at different cycles of Mo₂ QDs-CNTs/S@NH. (f) Nyquist plots of CNTs/S, Mo₂ QDs-CNTs/S and Mo₂ QDs-CNTs/S@NH electrodes. (g) The long-term cycling performance of the Mo₂ QDs-CNTs/S@NH cathode at 2.0C.

efficiency is higher than 97.6%, proving that the shuttling effect has been efficiently suppressed. The results indicate that the remarkable cycling stability of MoS_2 QDs-CNTs/S@NH at high current densities benefit from the well-designed structures assembled by the number of MoS_2 QD decorated on CNTs interwoven networks with ultrathin Ni(OH)_2 coating. This structure can efficiently capture polysulfides through synergistic adsorption and catalysis, which ensures high electrode conductivity, accommodates volume changes, and suppresses shuttle effects. Nanosizing MoS_2 is the most feasible method to increase its specific surface area and the number of active sites. Due to the fact that the active sites in MoS_2 are mainly located at the edge sites, reasonable control of its morphology and size is necessary to obtain MoS_2 nanomaterials rich in edge sites and maximize the exposure of active sites. Many studies have also demonstrated that MoS_2 nanostructures exhibit good binding strength with polysulfides. As an activated catalyst, it not only promotes the redox kinetics of polysulfides but also facilitates the effective decomposition of lithium sulfide.

4 Conclusion

In summary, a new nanocomposite of MoS_2 QDs-CNTs/S@NH was ingeniously designed as both a sulfur host and catalyst to enhance electrochemical kinetics and trapped LiPSs for Li-S batteries. Combining the advantage of polar and catalytic MoS_2 QDs with the highly conductive CNTs network, the LiPSs would probably be adsorbed by a large number of unsaturated bonds of MoS_2 QDs and physical adsorption of conductive CNTs. The thin Ni(OH)_2 coating forms a protective layer, which not only prevents sulfur loss but also effectively captures LiPSs through chemical interactions. The Li-S battery containing MoS_2 QDs-CNTs/S@NH as cathode shows outstanding long-term cycling stability and good rate performance. During 800 cycles at 2C, a capacity decay rate of 0.051% per cycle was obtained. This work provides a reasonable design of a sulfur host and shows its potential for application in Li-S batteries.

Data availability

Data and research materials will be available on request. The data supporting this article have been included in the article and its ESI.†

Author contributions

Meng Wei: conceptualization, writing – review & editing; Hanqing Lu: investigation; Zhen Wang: formal analysis; Bao-wen Lu, Pengtao Wang: resources; Xinxin Zhang, Bingjie Feng, Yingjie Xie: validation, Tao Zhang, Guanghui Liu, Song Xu: methodology.

Conflicts of interest

The authors declare no conflict of interest.

Acknowledgements

This work was supported by the Science and Technology Project of Henan Province (No. 232102241002); Aeronautical Science Foundation of China (No. 2022Z040055001); 2023 Henan University Research Teaching project; the Natural Science Foundation of Henan Province (222300420576); Graduate Education Innovation Program Fund of Zhengzhou University of Aeronautics (Grant No. 2023CX77).

References

- 1 C. Zhao, Y. Huang, B. Jiang, Z. Chen, X. Yu, X. Sun, H. Zhou, Y. Zhang and N. Zhang, *Adv. Energy Mater.*, 2023, **14**, 2302586.
- 2 X. Kang, T. He, R. Zou, S. Niu, Y. Ma, F. Zhu and F. Ran, *Small*, 2023, **20**, 2306503.
- 3 P. Salimi, E. Venezia, S. Taghavi, S. Tieuli, L. Carbone, M. Prato, M. Signoretto, J. Qiu and R. Proietti Zaccaria, *Energy Environ. Mater.*, 2023, 100316.
- 4 J. Li, Z. Wang, K. Shi, Y. Wu, W. Huang, Y. Min, Q. Liu and Z. Liang, *Adv. Energy Mater.*, 2023, 2303546.
- 5 Y. Kong, L. Wang, M. Mamoor, B. Wang, G. Qu, Z. Jing, Y. Pang, F. Wang, X. Yang, D. Wang and L. Xu, *Adv. Mater.*, 2023, **36**, 2310143.
- 6 X. Zhu, T. Bian, X. Song, M. Zheng, Z. Shen, Z. Liu, Z. Guo, J. He, Z. Zeng, F. Bai, L. Wen, S. Zhang, J. Lu and Y. Zhao, *Angew. Chem., Int. Ed.*, 2023, **62**, e202315087.
- 7 Z. Li, I. Sami, J. Yang, J. Li, R. V. Kumar and M. Chhowalla, *Nat. Energy*, 2023, **8**(1), 84–93.
- 8 Y.-G. Lee, S. Fujiki, C. Jung, N. Suzuki, N. Yashiro, R. Omoda, D.-S. Ko, T. Shiratsuchi, T. Sugimoto, S. Ryu, J. H. Ku, T. Watanabe, Y. Park, Y. Aihara, D. Im and I. T. Han, *Nat. Energy*, 2020, **5**(4), 299–308.
- 9 Y. Yan, P. Zhang, Z. Qu, M. Tong, S. Zhao, Z. Li, M. Liu and Z. Lin, *Nano Lett.*, 2020, **20**(10), 7662–7669.
- 10 J. S. Yeon, S. Yun, J. M. Park and H. S. Park, *ACS Nano*, 2019, **13**(5), 5163–5171.
- 11 M. Jana, R. Xu, X.-B. Cheng, J. S. Yeon, J. M. Park, J.-Q. Huang, Q. Zhang and H. S. Park, *Energy Environ. Sci.*, 2020, **13**(4), 1049–1075.
- 12 S. Wang, Z. Wang, F. Chen, B. Peng, J. Xu, J. Li, Y. Lv, Q. Kang, A. Xia and L. Ma, *Nano Res.*, 2023, **16**(4), 4438–4467.
- 13 W. Zhang, H. Pan, N. Han, S. Feng, X. Zhang, W. Guo, P. Tan, S. Xie, Z. Zhou, Q. Ma, X. Guo, A. Vlad, M. Wübbenhurst, J. Luo and J. Fransaer, *Adv. Energy Mater.*, 2023, **13**(43), 2301551.
- 14 L. Ren, K. Sun, Y. Wang, A. Kumar, J. Liu, X. Lu, Y. Zhao, Q. Zhu, W. Liu, H. Xu and X. Sun, *Adv. Mater.*, 2024, **36**, 2310547.
- 15 P. R. Adhikari, E. Lee, L. Smith, J. Kim, S. Shi and W. Choi, *RSC Adv.*, 2023, **13**(14), 9402–9412.
- 16 Z. Song, L. Wang, W. Jiang, M. Pei, B. Li, R. Mao, S. Liu, T. Zhang, X. Jian and F. Hu, *Adv. Energy Mater.*, 2023, **14**, 2302688.
- 17 S. Liu, X. Xia, S. Deng, D. Xie, Z. Yao, L. Zhang, S. Zhang, X. Wang and J. Tu, *Adv. Mater.*, 2018, **31**(3), 1806470.



18 M. S. Md Zaini, N. F. Anuar, S. A. M. Al-Junid and S. S. A. Syed-Hassan, *Mater. Sci. Energy Technol.*, 2023, **6**, 205–225.

19 X. Meng, S. Chen, S. Hong, L. Zheng, X. Liu, G. Shi, C. W. Bielawski and J. Geng, *Chem. Eng. J.*, 2024, **486**, 150241.

20 X. Jiao, J. Hu, Y. Zuo, J. Qi, W. Yan and J. Zhang, *Nano Energy*, 2024, **119**, 109078.

21 J. Qin, R. Wang, P. Xiao and D. Wang, *Adv. Energy Mater.*, 2023, **13**(26), 2300611.

22 Y. Huang, L. Zhang, J. Ji, C. Cai and Y. Fu, *Energy Storage Mater.*, 2024, **64**, 103065.

23 B. Liu, H. Gu, J. F. Torres, Z. Yin and A. Tricoli, *Energy Environ. Sci.*, 2024, **17**, 1073–1082.

24 Z. Du, X. Chen, W. Hu, C. Chuang, S. Xie, A. Hu, W. Yan, X. Kong, X. Wu, H. Ji and L.-J. Wan, *J. Am. Chem. Soc.*, 2019, **141**(9), 3977–3985.

25 J. Billaud, F. Bouville, T. Magrini, C. Villevieille and A. R. Studart, *Nat. Energy*, 2016, **1**(8), 1–6.

26 X. Meng, X. Liu, X. Fan, X. Chen, S. Chen, Y. Meng, M. Wang, J. Zhou, S. Hong, L. Zheng, G. Shi, C. W. Bielawski and J. Geng, *Adv. Sci.*, 2021, **9**(3), 2103773.

27 J. Zhou, X. Chen, W. Gong, X. Meng, C. Chen, X. Zhou, M. Wang, K. N. Hui and J. Geng, *J. Energy Storage*, 2024, **75**, 109505.

28 X. Gu, S. Zhang and Y. Hou, *Chin. J. Chem.*, 2016, **34**(1), 13–31.

29 J. Castillo, A. Soria-Fernández, S. Rodriguez-Peña, J. Rikarte, A. Robles-Fernández, I. Aldalur, R. Cid, J. A. González-Marcos, J. Carrasco, M. Armand, A. Santiago and D. Carriazo, *Adv. Energy Mater.*, 2023, **14**(1), 2302378.

30 J. K. Kim, Y. Choi, E. D. Jeong, S. J. Lee, H. G. Kim, J. M. Chung, J.-S. Kim, S.-Y. Lee and J.-S. Bae, *Nanomaterials*, 2022, **12**(20), 3605.

31 Y. Chang, Y. Ren, L. Zhu, Y. Li, T. Li and B. Ren, *Electrochim. Acta*, 2022, **420**, 140454.

32 X. Zhang, *IOP Conf. Ser.: Earth Environ. Sci.*, 2021, **781**(4), 042051.

33 R. Mori, *J. Solid State Electrochem.*, 2023, **27**(4), 813–839.

34 F. Shi, L. Zhai, Q. Liu, J. Yu, S. P. Lau, B. Y. Xia and Z.-L. Xu, *J. Energy Chem.*, 2023, **76**, 127–145.

35 S. Zeng, G. M. Arumugam, X. Liu, Y. Yang, X. Li, H. Zhong, F. Guo and Y. Mai, *Small*, 2020, **16**(39), 2001027.

36 T. T. Zhang, C. Y. Yang, J. Qu, W. Chang, Y. H. Liu, X. Z. Zhai, H. J. Liu, Z. G. Jiang and Z. Z. Yu, *Chem.-Eur. J.*, 2022, **28**(31), e202200363.

37 P. Zeng, Z. Zhou, B. Li, H. Yu, X. Zhou, G. Chen, B. Chang, M. Chen, H. Shu, J. Su and X. Wang, *ACS Appl. Mater. Interfaces*, 2022, **14**(31), 35833–35843.

38 W. Zhao, L.-C. Xu, R. Li, Y. Guo, Z. Yang, R. Liu and X. Li, *Mater. Today Commun.*, 2022, **30**, 103196.

39 X. Liu, H. Rao, K. Sun, H. Gou, T. Lu and Y. Qian, *Appl. Surf. Sci.*, 2022, **599**, 154022.

40 J. Tang, C. Jin, L. Huo, S. Du, X. Xu, Y. Yan, K. Jiang, L. Shang, J. Zhang, Y. Li, Z. Hu and J. Chu, *ACS Appl. Mater. Interfaces*, 2022, **14**(45), 50870–50879.

41 Y. Liu, T. Lei, Y. Li, W. Chen, Y. Hu, J. Huang, J. Chu, C. Yan, C. Wu and C. Yang, *J. Power Sources*, 2023, **556**, 232501.

42 J. Zu, W. Jing, X. Dai, Z. Feng, J. Sun, Q. Tan, Y. Chen and Y. Liu, *J. Alloys Compd.*, 2023, **933**, 167767.

43 C. Zhao, Y. Zhou, T. Shi, H. Yin, C. Song, L. Qin, Z. Wang, H. Shao and K. Yu, *J. Alloys Compd.*, 2023, **934**, 167975.

44 Y. Lu, M. Zhao, Y. Yang, M. Zhang, N. Zhang, H. Yan, T. Peng, X. Liu and Y. Luo, *Nanoscale Horiz.*, 2022, **7**(5), 543–553.

45 L. Sun, W. Gong, J. Zhou, J. Zhang, C. Chen, X. Meng, X. Han, H. Mai, C. W. Bielawski and J. Geng, *J. Colloid Interface Sci.*, 2024, **653**, 1694–1703.

46 G. Wen, X. Zhang, Y. Sui, K. Rao, J. Liu, S. Zhong and L. Wu, *Chem. Eng. J.*, 2022, **430**, 133041.

47 X. Yang, S. Chen, W. Gong, X. Meng, J. Ma, J. Zhang, L. Zheng, H. D. Abruña and J. Geng, *Small*, 2020, **16**(48), 2004950.

48 F. Li, J. Li, Z. Cao, X. Lin, X. Li, Y. Fang, X. An, Y. Fu, J. Jin and R. Li, *J. Mater. Chem. A*, 2015, **3**(43), 21772–21778.

49 H. Wei, Y. Ding, H. Li, Q. Zhang, N. Hu, L. Wei and Z. Yang, *Electrochim. Acta*, 2019, **327**, 134994.

50 Y. Xia, H. Zhong, R. Fang, C. Liang, Z. Xiao, H. Huang, Y. Gan, J. Zhang, X. Tao and W. Zhang, *J. Power Sources*, 2018, **378**, 73–80.

51 B. Yu, A. Huang, D. Chen, K. Srinivas, X. Zhang, X. Wang, B. Wang, F. Ma, C. Liu, W. Zhang, J. He, Z. Wang and Y. Chen, *Small*, 2021, **17**(23), 2100460.

52 H. Zhang, L. Yang, P. Zhang, C. Lu, D. Sha, B. Yan, W. He, M. Zhou, W. Zhang, L. Pan and Z. Sun, *Adv. Mater.*, 2021, **33**(21), 2008447.

53 H. Wang, S.-A. He, Z. Cui, C. Xu, J. Zhu, Q. Liu, G. He, W. Luo and R. Zou, *Chem. Eng. J.*, 2021, **420**, 129693.

